

# Room-Temperature Ferromagnetism and Extraordinary Hall Effect in Nanostructured Q-Carbon: Implications for Potential Spintronic Devices

Anagh Bhaumik,<sup>†</sup> Sudhakar Nori,<sup>†</sup> Ritesh Sachan,<sup>†,‡</sup> Siddharth Gupta,<sup>†</sup> Dhananjay Kumar,<sup>§</sup> Alak Kumar Majumdar,<sup>||</sup> and Jagdish Narayan<sup>\*,†</sup>

<sup>†</sup>Department of Materials Science and Engineering, Centennial Campus North Carolina State University, Raleigh, North Carolina 27695-7907, United States

<sup>‡</sup>Materials Science Division, Army Research Office, Research Triangle Park, North Carolina 27709, United States

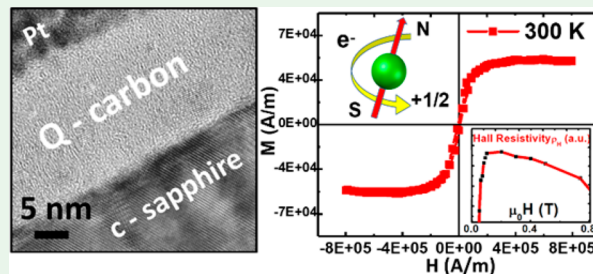
<sup>§</sup>Department of Materials Science and Engineering, North Carolina Agricultural and Technical State University, Greensboro, North Carolina 27401, United States

<sup>||</sup>Ramakrishna Mission Vivekananda University, Belur Math, Howrah, West Bengal 711202, India

## Supporting Information

**ABSTRACT:** We report extraordinary Hall effect and room-temperature ferromagnetism in undoped Q-carbon, which is formed by nanosecond pulsed laser melting and subsequent quenching process. Through detailed structure–property correlations in Q-carbon thin films, we show the excess amount of unpaired electrons near the Fermi energy level give rise to interesting magnetic and electrical properties. The analysis of the extraordinary Hall effect in Q-carbon follows nonclassical “side-jump” electronic scattering mechanism. The isothermal field-dependent magnetization plots confirm room-temperature ferromagnetism in Q-carbon with a finite coercivity at 300 K and a Curie temperature of 570 K, obtained by the extrapolation of the fits to experimental data using modified Bloch’s law. High-resolution scanning electron microscopy and transmission electron microscopy clearly illustrate the formation of Q-carbon and its subsequent conversion to single-crystalline diamond. Further, we found n-type conductivity in Q-carbon in the entire temperature range from 10 to 300 K based on the extraordinary Hall coefficient versus magnetic field experiments. This discovery of interesting magnetic and electron transport properties of Q-carbon show that nonequilibrium synthesis technique using super undercooling process can be used to fabricate new materials with greatly enhanced physical properties and functionalities. The observed robust room-temperature ferromagnetism coupled with extraordinary Hall effect in Q-carbon will find potential applications in carbon-based spintronics.

**KEYWORDS:** ferromagnetism, quenched carbon, Raman spectroscopy, electron energy-loss spectroscopy, extraordinary Hall effect, n-type conductivity, spintronics, magnetotransport



Carbon-based materials possess versatile physical and chemical properties.<sup>1</sup> The outer 2s and 2p shells in a carbon atom can hybridize in three different ways to form sp, sp<sup>2</sup>, and sp<sup>3</sup> orbital wave functions. For the carbon materials consisting of a mixture of sp<sup>2</sup> and sp<sup>3</sup> bonding types, a dominant factor in determining their physical properties is the sp<sup>2</sup>/sp<sup>3</sup> ratio. Graphite is considered to be one of the strongest diamagnetic materials among naturally occurring substances. This is due to the large orbital diamagnetism and small effective electronic mass in its band structure.<sup>2</sup> The diamagnetic effect is also observed in graphene.<sup>3</sup> Fullerenes (C<sub>60</sub>) also exhibit diamagnetic and paramagnetic ring currents due to the existence of mobile (delocalized) π electrons. With a few exceptions, most of the carbon allotropes exhibit a diamagnetic susceptibility.<sup>2</sup> Recently, an extremely interesting coexistence of superconducting and ferromagnetic states have been observed in hydrogenated boron-doped nanodiamond.<sup>4</sup> The ferromag-

netic properties of carbon-based materials arise primarily due to (i) radicals that form chainlike structures and interact with each other (long-range and short-range interactions),<sup>5,6</sup> (ii) carbon mixtures comprising of the fractions of sp<sup>2</sup> and sp<sup>3</sup> hybridized states,<sup>7,8</sup> (iii) carbon structures consisting of impurities, namely, P, N, and B,<sup>9–11</sup> and (iv) irradiation of graphite and highly oriented pyrolytic graphite (HOPG).<sup>12,13</sup> Yet surprisingly, theory predicts (assuming each carbon atom has a spin of one unpaired electron that contributes to ferromagnetic ordering) much higher values of saturation magnetization  $M_s$  than those observed experimentally (only 0.1% of the theoretical value is observed).<sup>14</sup> Atomic force microscopy

Received: November 25, 2017

Accepted: January 23, 2018

Published: January 23, 2018

(AFM) and scanning tunneling microscopy (STM) studies also suggest that topological defects, such as functional groups and point defects, perturb the electronic properties of graphite thereby giving rise to its magnetic properties.<sup>15</sup> In addition, the magnetic properties of pure and doped graphene can also be explained by itinerant ferromagnetism of dilute two-dimensional electron gas with the strong Coulomb interaction between electrons.<sup>16</sup> At the edge states (and defect sites), there occur electron–electron interactions that cause magnetic polarization. The examination of the electron–electron interaction effects in the Hubbard model also reveals a possibility of spontaneous magnetic ordering in the nanometer-scale fragments of graphite.<sup>17</sup> This also causes the formation of excitonic states that assist in the alignment of the unpaired electrons thereby giving rise to weak ferromagnetism in carbon-based materials.<sup>18</sup> Ferromagnetism is also reported in N-doped polycrystalline diamond thin films due to the presence of  $sp^3$ – $sp^2$  electronic moieties.<sup>19</sup> This reduces the orbital Coulomb repulsion thereby causing ferromagnetism.<sup>19</sup> The synthesis of hybrid carbon-based photochromic and electrochromic molecules are also being vigorously pursued to fabricate multifunctional molecular materials.<sup>20</sup>

In a search for bulk ferromagnetism in carbon, we synthesized a novel amorphous phase of carbon by quenching the undercooled liquid carbon,<sup>21</sup> which is distinctly different from other thermodynamically stable forms of carbon, namely, graphite, diamond, liquid, and vapor.<sup>22</sup> The synthesized phase Q-carbon is ferromagnetic, electron-emissive, *harder* than diamond, and can be transformed into single-crystal diamond at room temperature and ambient pressure.<sup>21,23</sup> This phase is a new state of solid carbon with a higher mass density than amorphous carbon and comprises of a mixture of mostly fourfold  $sp^3$  (75–85%) and the rest threefold  $sp^2$  bonded carbon (with distinct entropy).<sup>23</sup> The formation of Q-carbon is accomplished by nanosecond laser melting of amorphous carbon in a super-undercooled state and subsequently quenching the molten carbon. The process of pulsed laser irradiation causes the electrons to be excited into the conduction band. These excited electrons transfer their energy quickly to phonons, leading to rapid heating and melting. The formation of Q-carbon depends on the laser energy density, physical properties of the as-deposited amorphous C film, and the substrate. The molten state of carbon is metallic,<sup>24</sup> and thereby in the structure of Q-carbon, the C atoms can be densely packed. This packing causes an increase in the hardness, density, and the electron concentration near the Fermi energy level in Q-carbon. The process of super undercooling and subsequent quenching can transform the as-deposited amorphous carbon into Q-carbon, nanodiamond, microdiamond, and/or large-area diamond. The thermal conductivities of as-deposited diamond-like carbon (DLC) or amorphous C thin films and the substrate (sapphire) play a vital role in the formation of Q-carbon. A high quenching rate leads to large solidification velocity thereby promoting the formation of densely packed amorphous Q-carbon structure. We also demonstrated the formation of single-crystal diamond on lattice and planar matched substrates (Cu, sapphire) using the pulsed laser annealing technique.<sup>25–27</sup> These transformations are dictated by the undercooling temperatures and quenching rates, according to the free-energy versus temperature diagram.<sup>23</sup> The formation of supersaturated alloys of Si and Ge by using pulsed laser annealing technique have been extensively studied.<sup>28–30</sup> The undercooling in Si and Ge was

estimated to be 241 and 336 K, respectively.<sup>31</sup> In the case of amorphous C, the undercooling values can be well over 1000 K. The undercooling phenomenon in carbon (graphite) was not followed with any vigor due to the understanding from the equilibrium phase diagram, according to which graphite converts into vapor above  $\sim 4000$  K and at low pressures.<sup>22</sup> Q-Carbon has a high fraction of  $sp^3$  hybridized electronic states and dangling bonds that contain delocalized electrons. The electronic structure of Q-carbon consists of overlapping orbitals of  $sp^2$  and  $sp^3$  electronic states and is expected to possess exciting physical, chemical, and catalytic properties. Undoped Q-carbon is ferromagnetic, which upon doping turns paramagnetic. B-Doped (25 atom %) Q-carbon exhibits high-temperature Bardeen–Cooper–Schrieffer (BCS) superconductivity.<sup>32</sup> Spintronic applications demand coupling of magnetic and transport properties in robust ferromagnets.<sup>33</sup> Though there are several reports on magnetotransport in various materials,<sup>34,35</sup> such studies are not available for carbon-based materials. Therefore, magnetotransport properties of carbon-based materials should be investigated to confirm that the charge carriers are indeed coupled with the magnetic spins, thereby giving rise to novel functionalities. The observance of extraordinary Hall effect in thin films also suggests that the charge carriers interact with the ferromagnetic coupling. The coexistence of room-temperature ferromagnetism and extraordinary Hall effect in thin films is extremely important, because the ferromagnetically spin-polarized carriers can be controlled electronically thereby leading to ultrafast switching device applications in the field of multifunctional electronics.

In the present study, we focused on structure–property correlations using various state-of-the-art measurements and characterization techniques to understand the ferromagnetism and extraordinary Hall effect in Q-carbon. The structure and properties of Q-carbon are studied by employing secondary ion mass spectroscopy (SIMS), electron energy-loss spectroscopy (EELS), high-resolution transmission electron microscopy (HRTEM), Raman spectroscopy, X-ray diffraction (XRD), magnetic force microscopy (MFM), and field emission scanning electron microscopy (FESEM). The formation of Q-carbon is also simulated by employing the solid laser interaction in materials (SLIM) software developed by Singh and Narayan.<sup>36</sup> We examined the ferromagnetic behavior of Q-carbon using the temperature-dependent magnetic susceptibility measurements in superconducting quantum interference device (SQUID). To study the nonclassical electron scattering mechanism in Q-carbon, five-probe electrical measurements to measure Hall voltage were performed in the physical property measurement system (PPMS). With this study, we propose that the nonequilibrium undercooling assisted synthesis methods can be used to fabricate novel materials, which possess greatly enhanced physical properties.

## METHODS

Amorphous carbon thin films were deposited onto c-sapphire using pulsed laser deposition with a thickness ranging from 50 to 500 nm in the temperature range of 30–300 °C and  $4.0 \times 10^{-7}$  Torr base pressure. During the pulsed laser deposition, nanosecond laser pulses of KrF (laser wavelength = 248 nm, pulse duration = 25 ns) with an energy density of 2.5–3.0 J cm<sup>-2</sup> are used. Subsequently, these amorphous carbon films are irradiated with nanosecond ArF excimer laser (laser wavelength = 193 nm, pulse duration = 20 ns) pulses using laser energy density 0.6–1.0 J cm<sup>-2</sup>. The pulsed laser annealing technique melts the amorphous carbon thin film in a highly super-undercooled state that can be quenched rapidly. The pulsed laser

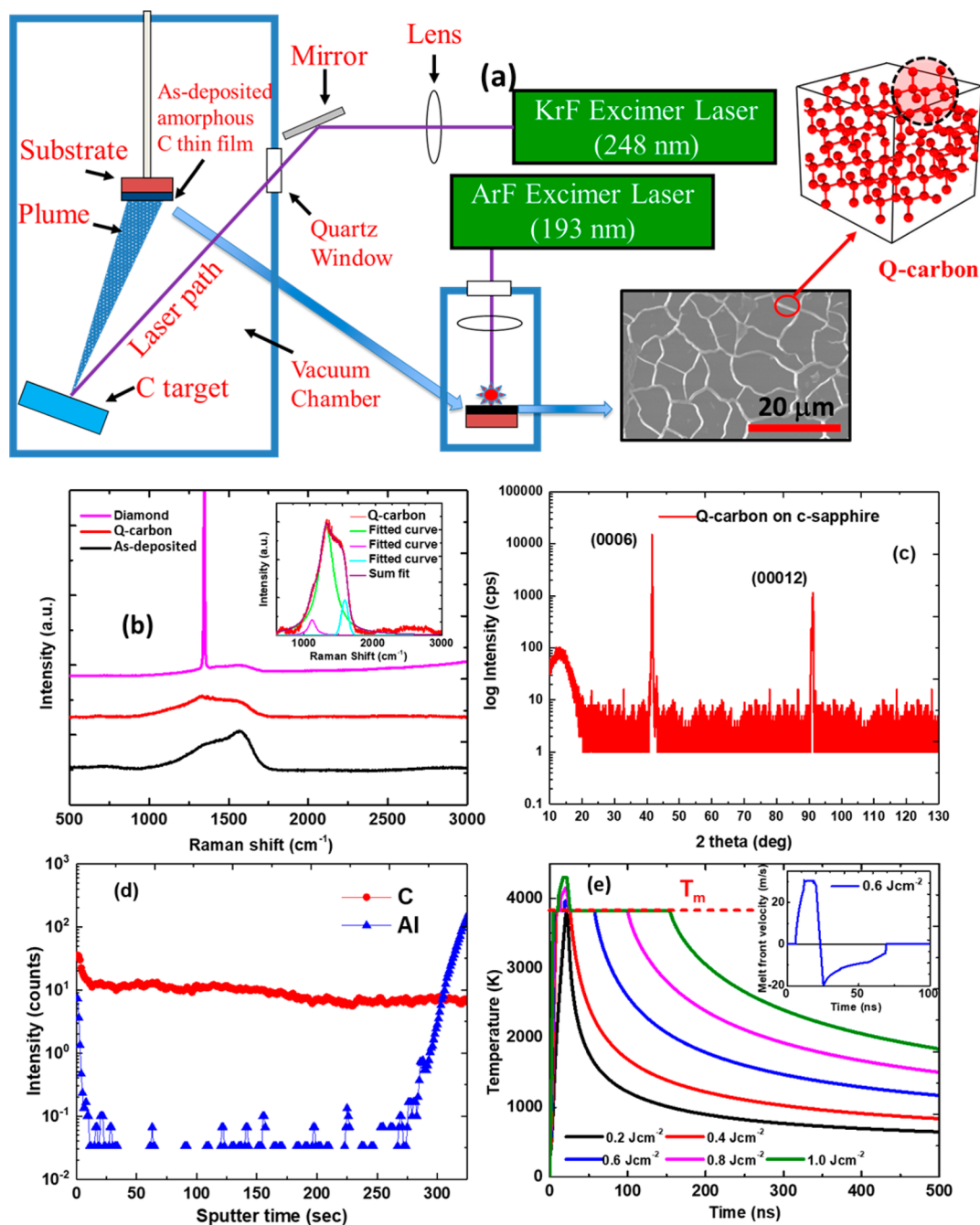


**Figure 1.** (a) Schematic of the synthesis of amorphous Q-carbon using pulsed laser deposition followed by PLA technique; (b) Raman spectroscopy of as-deposited amorphous C thin film, Q-carbon, and diamond formed from Q-carbon after PLA; (c) XRD of Q-carbon on c-sapphire; (d) SIMS profile of Q-carbon; and (e) SLIM profiles at various laser energy densities. The red dotted region in (a) shows random DCL ( $sp^3$ ) tetrahedra with  $sp^2$  bonding at the interfaces in Q-carbon. The inset in (b) shows the peak fitted Raman spectrum of Q-carbon indicating a 75%  $sp^3$ . The inset in (e) shows the melt-front velocity (20 m/sec) when  $0.6 \text{ J cm}^{-2}$  laser energy density is used.

annealing process is completed within 200–250 ns. This leads to conversion of amorphous carbon films into Q-carbon and/or micro and nanostructures of the diamond. This conversion is dependent on the degree of undercooling, rate of quenching, and solidification velocities during the pulsed laser annealing technique. Figure 1a depicts the schematic of the synthesis of amorphous Q-carbon using pulsed laser deposition followed by pulsed laser annealing. The characterization of the Q-carbon phase was performed using Raman spectroscopy, SIMS, EELS, FESEM, HRTEM, SQUID magnetometry, PPMS, MFM, and XRD. XRD ( $\lambda = 1.5406 \text{ \AA}$ ) combined with SIMS techniques rule out the presence of ferromagnetic impurities in a large-area and parts per million level in Q-carbon. Figure 1d illustrates the

SLIM theoretical calculations that indicate a melt-front velocity of 20 m/sec, essential for the formation of Q-carbon. The structure of Q-carbon and its conversion to diamond have also been reported previously.<sup>23</sup> Alfa300R superior confocal Raman spectroscope with a lateral resolution less than 200 nm was employed to characterize the Raman-active vibrational modes in Q-carbon and diamond. Crystalline Si with its characteristic Raman peak at  $520.6 \text{ cm}^{-1}$  was used to calibrate Raman spectra. High-resolution SEM in immersion mode with a sub-nanometer resolution was performed using FEI Verios 460L SEM to characterize the as-deposited and the laser-irradiated films. Time-of-flight secondary ion mass spectrometer (TOF-SIMS) with a lateral resolution of less than 300 nm was used to detect the

presence of C in addition to Al and other trace impurities in the Q-carbon thin films. FEI Quanta 3D FEG with dual beam technology employing both electron and ion beam guns was used for preparing cross-sectional TEM samples. A low-energy ion beam (5 kV, 10 pA) was used to clean the focused ion beam (FIB) surface damage. Aberration-corrected STEM-FEI Titan 80–300 was used in conjunction with electron energy-loss spectroscopy (EELS with a resolution of 0.15 eV) to acquire EELS spectra of diamond and Q-carbon thin films. The electron probe current used in the experiment was  $38 \pm 2$  pA. The EELS data were acquired with a collection angle of 28 mrad. Quantum Design magnetic property measurement system (MPMS3) was used to measure magnetic properties of thin films. Vibrating sample magnetometer (VSM) and direct-current (DC) modes were used for measuring field-dependent magnetization. The magnetic measurements were made with samples mounted parallel to the magnetic field. We measured the thickness of Q-carbon using the high-resolution cross-sectional transmission electron microscopy, and it is represented in the Figure 2c. The thickness is calculated as 20 nm.

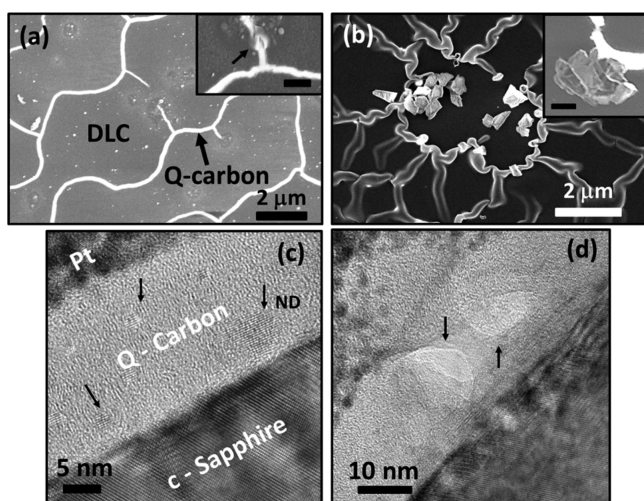


**Figure 2.** (a) High-resolution SEM images showing the formation of Q-carbon with the inset indicating (by the black arrow) a first-order phase transformation during the formation of Q-carbon; (b) SEM image indicating formation of single-crystal diamonds at the Q-carbon triple points with the inset showing the formation of nanodiamonds (NDs) and microdiamonds from Q-carbon; (c) HRTEM image of Q-carbon showing the nucleation of NDs; and (d) HRTEM image indicating (by black arrows) the formation of diamond facets. The scale bars in the insets of (a, b) are 500 and 200 nm, respectively.

The volume of the sample is therefore calculated as  $3.2 \times 10^{-7}$  cm<sup>3</sup>. Taking the density as 3.51 g/cm<sup>3</sup>, the normalized magnetization values were calculated. Five probe electrical measurements are performed on Q-carbon thin films using PPMS to probe the nonclassical electronic scattering mechanism. The misalignment voltage was adjusted to less than 0.1  $\mu$ V prior to data acquisition at each temperature. The sign of the Hall voltage ( $V_H$ ) was calibrated using a standard Fe sample (positive  $V_H$  at 300 K). Asylum Research MFP-3D Infinity AFM was employed for MFM imaging. MFM silicon probe with 50 nm Co–Cr coated tip was used for the MFM scans. The MFM image was taken with a delta height of 50 nm and was flattened to zeroth order to improve its contrast. The samples were stabilized on the granite platform in the Asylum Research MFP-3D instrument for 24 h prior to MFM measurements.

## RESULTS AND DISCUSSION

Figure 1b depicts the Raman spectra from as-deposited DLC, Q-carbon, and diamond on sapphire performed using 532 nm laser excitation. The Q-carbon is formed on the substrate after a single laser pulse of ArF laser (energy density: 0.6 J cm<sup>-2</sup>). The

nucleation of nano and microdiamonds is also achieved during the formation of Q-carbon, which contains the seeds ( $sp^3$  hybridized electronic states) of diamond nuclei. Subsequent pulsed laser annealing of Q-carbon can also lead to the formation of nano, micro, and large-area single-crystal diamond.<sup>23</sup> The Raman peak of the diamond grown from the Q-phase is centered at 1334 cm<sup>-1</sup>. This mode corresponds to the vibration of the two interpenetrating cubic sublattices present in the diamond.<sup>37</sup> The inset of Figure 1b represents the peak-fitted Raman spectra of Q-carbon. The Raman spectrum of Q-carbon can be deconvoluted to a diamond peak at 1329 cm<sup>-1</sup> with a broad peak around 1350 cm<sup>-1</sup>, a small peak at 1140 cm<sup>-1</sup> that is associated with the strained  $sp^2$  carbon at the interface and the graphitic peak at 1560 cm<sup>-1</sup>. The peak fitting of the Q-carbon Raman spectra yields a 75–80% of  $sp^3$  hybridized electronic states. From preliminary electron diffraction experiments, we derive that Q-carbon is formed as result of random packing of carbon tetrahedra with packing efficiency of over 80% with  $sp^3$  bonding within and  $sp^2$  between them. The blue shift of the diamond peak in the Q-carbon Raman spectrum is associated with the strains generated after the quenching process. The small peak at 1040 cm<sup>-1</sup> is due to the presence of  $sp^2$  bonds on the surface of nanodiamonds, which are present in the structure of Q-carbon. The increase in the full width at half-maximum (fwhm) of the diamond peak that is associated with Q-carbon can also be due to phonon confinement effects and the presence of nanodiamonds in the Q-carbon structure.

Figure 1c represents the XRD spectrum of amorphous Q-carbon grown on c-sapphire. The diffraction peaks at  $2\theta = 41.6^\circ$  and  $91.1^\circ$  correspond to (0006) and (00012) sapphire. The absence of any other peaks in the logarithmic plot of XRD spectrum (up to  $2\theta = 130^\circ$ ) indicates that the Q-carbon thin films are pristine in nature. Figure 1d indicates the SIMS profile of Q-carbon. There are no impurity elements at parts per million level in the Q-carbon thin films. Very recently we also demonstrated homogeneous melting of B-doped carbon using the nanosecond pulsed laser annealing technique.<sup>32,38,39</sup> From boron distribution, the diffusivities were determined to be  $\sim 1 \times 10^{-4}$  cm<sup>2</sup>/V/sec, which confirmed the melting of carbon. The pulsed laser annealing (PLA) process is an ultrafast technique (completed in less than 250 ns), which minimizes contamination of impurities from the atmosphere. The calculation of threshold energy is crucial for this study, as it determines the minimum laser energy required for melting amorphous carbon, which leads to the formation of Q-carbon. We used the SLIM programming<sup>36</sup> to simulate the laser–solid interactions. The initial layered structure consists of amorphous carbon (75%  $sp^3$ )/sapphire. The threshold energy ( $E_{th}$ ) required for melting few layers of amorphous carbon/sapphire is calculated as 0.4 J cm<sup>-2</sup>.<sup>36</sup> Figure 1e depicts the temperature versus time (in ns) plots for various energy densities, which are calculated using the SLIM program by employing a nanosecond laser ( $\lambda = 193$  nm, laser width = 20 ns). As it is evident from the plots, melting of the as-deposited amorphous carbon layer occurs when energy densities above 0.4 J cm<sup>-2</sup> are used. The red dotted line indicates the melting temperature ( $T_m$ ) of carbon. The thickness of the melted region varies linearly with the pulse energy density. The surface starts to melt slowly due to the sudden change in reflectivity during the phase transition. As the laser pulse terminates, the melt front recedes back to the surface. The initial stages of solidification see a low velocity, but it quickly reaches the maximum when the steady-state

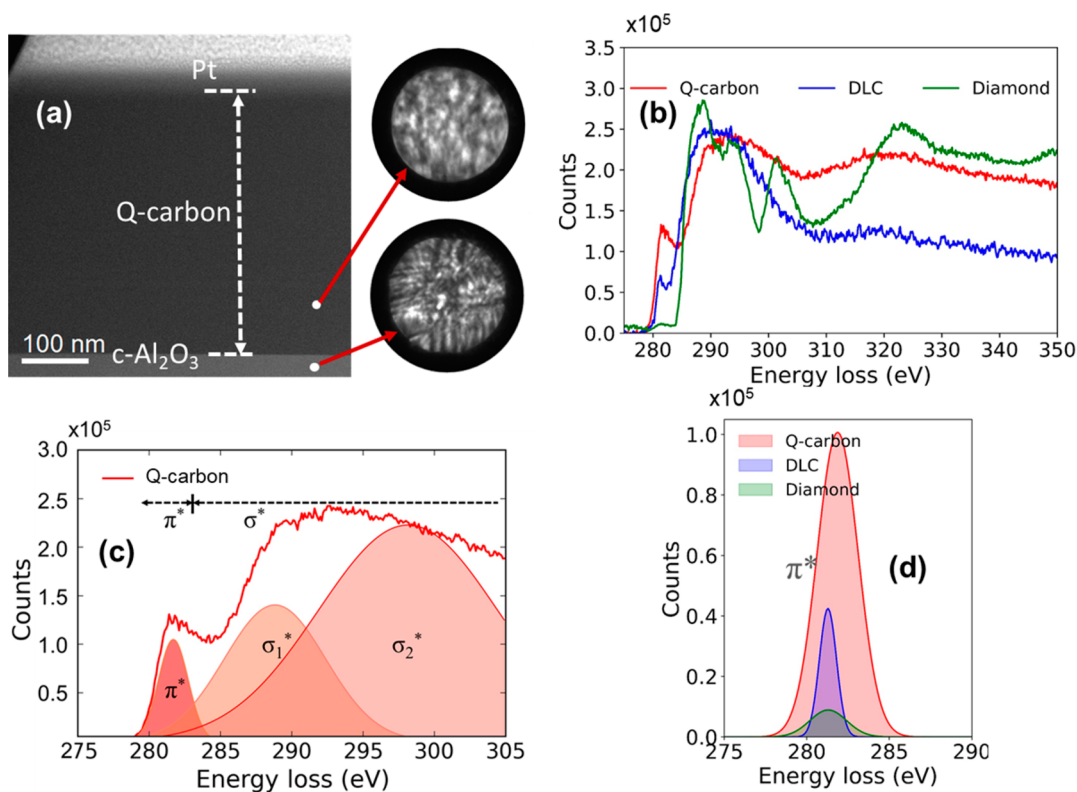


**Figure 3.** (a) HAADF image of Q-carbon on c-sapphire along with the Ronchigram pattern confirming amorphous and crystalline nature of Q-carbon and c-sapphire, respectively; (b) EELS spectra of Q-carbon, as-deposited DLC and diamond; (c) representative fitting routine performed on Q-carbon EELS spectrum; and (d) the fitted  $\pi^*$  peaks indicating an increase in the density of the electronic states in Q-carbon as compared to DLC and diamond.

condition is achieved. The melt front velocity is estimated to be 20 m/sec for  $0.6 \text{ J cm}^{-2}$ , as shown in the inset of Figure 1e. These calculations involve an extremely accurate finite difference method to calculate the melt depth and temperature profile in the laser-annealed samples thereby providing valuable insights to the formation of Q-carbon.

Figure 2a,b represents high-resolution SEM images of Q-carbon and formation of diamond from Q-carbon, respectively. The super-undercooled carbon is formed near the film–substrate interface. Subsequent quenching of this structure leads to the formation of a filamentary structure of Q-carbon. The formation of these cellular structures (Figure 2a) indicates an interfacial instability at the solid–liquid interface.<sup>23,40</sup> The formation of these cellular structures in Q-carbon can also be controlled by thermal conductivity through the variation of  $sp^3$  fraction in the as-deposited amorphous carbon sample. The inset of Figure 2a illustrates the formation of Q-carbon from the as-deposited amorphous C layer. The sharp interface (as shown by the black arrow) corresponds to a first-order phase transformation (of amorphous Q-carbon to diamond transformation). The Q-carbon thus formed has  $\sim 75\text{--}80\%$   $sp^3$  bonding and also contains nanodiamond embedded in its structure. These nanodiamonds act as seeds or nucleating agents for subsequent nucleation of diamonds when the Q-carbon is irradiated with higher laser energy densities ( $0.6\text{--}1.0 \text{ J cm}^{-2}$ ). The formation of diamonds at the Q-carbon triple points is illustrated in Figure 2b. The inset of Figure 2b clearly shows the formation of nano and micro-sized crystals of diamond from the filamentary structure of Q-carbon. The nanodiamonds and microdiamonds can be formed either by heterogeneous (on the sapphire) or by homogeneous (on the

diamond) nucleation.<sup>21,23</sup> Figure 2c,d show the HRTEM images of Q-carbon grown on c-sapphire. It is evident from Figure 2c that Q-carbon has mostly amorphous structure with a few nanodiamonds embedded into it. The interplanar spacing of the nanodiamonds corresponds to the  $\{111\}$  lattice planes and is shown by black arrows in Figure 2c. In Figure 2d we show the formation of crystal facets of diamond from Q-carbon. Recently, we also reported the formation of nanoneedles, microneedles, and large-area diamond from Q-carbon.<sup>21,23,41</sup>

The details of bonding characteristics and electronic structure of Q-carbon were thoroughly investigated and compared with that of DLC and diamond. Figure 3a shows the high-angle annular dark field (HAADF) image of Q-carbon on c-sapphire substrate. The associated Ronchigram for the Q-carbon and c-sapphire are also presented in Figure 3a, demonstrating the amorphous and crystalline nature of the Q-carbon and sapphire, respectively. Figure 3b shows the EEL spectra obtained from Q-carbon, the parent DLC, and diamond, revealing the  $sp^3$  ( $\sigma^*$ ) and  $sp^2$  ( $\pi^*$ ) bonding characteristics. On the one hand, EEL spectra of Q-carbon and DLC consist of a sharp  $\pi^*$  peak (onset at 284 eV) and a broad  $\sigma^*$  peak (onset 290 eV). On the other hand, EEL spectrum for diamond shows only  $\sigma^*$ , as it purely consists of  $sp^3$  hybridized carbon atoms. With a fitting routine to the EELS,<sup>42</sup> the  $sp^3$  was estimated to be  $\sim 77\%$ , which is in excellent agreement with the Raman spectroscopy results ( $75\%$   $sp^3$ ) from Q-carbon. In the first look, EEL spectra of Q-carbon and DLC appear very similar (characteristic of amorphous C). However, upon closer observation, we discover that there is a significant difference between them. The  $\pi^*$  peak is sharper, and  $\sigma^*$  peak is broader, in Q-carbon as compared to the DLC.

It is worth noting that the EELS results in Q-carbon were repeatable across different sets of samples. Though it is expected that the parent DLC (containing  $\sim 60\%$   $sp^3$  based on Raman spectroscopy) should exhibit a higher intensity  $\pi^*$  peak in EELS as compared to Q-carbon ( $\sim 77\%$   $sp^3$ ), the results were totally inverse. A representative fitting routine performed on Q-carbon EELS spectrum is shown in Figure 3c. This demonstrates the fitting of one Gaussian in  $\pi^*$  and two in  $\sigma^*$  region. The Gaussian fitted  $\pi^*$  peaks for Q-carbon, parent DLC, and diamond are shown in Figure 3d, which unambiguously points out the highly enhanced intensity of  $\pi^*$  peak in Q-carbon. It is known that the long- and medium-range ordering of atoms in a material give rise to a sharper peak profile. This unexpected enhancement in  $\pi^*$  intensity in Q-carbon is attributed to the presence of a large number of unpaired spin electron density associated with distinct electronic states near the Fermi energy level.<sup>43</sup> The area under the  $\pi^*$  peak, which is related to the increase in the unpaired spins electrons, is increased by 80% in Q-carbon as compared to DLC. We propose that the unpaired spin electrons arise due to the presence of dangling C bonds in Q-carbon, which are formed through a highly nonequilibrium quenching process. This direct observation of the presence of a large number of unpaired spin electrons is envisaged to create unexpected magnetic and electronic behavior in Q-carbon, which is the primary objective of this study.

Figure 4a represents the field-dependent magnetization curves of Q-carbon performed at different temperatures (10, 100, 200, and 300 K). The magnetic curves ( $M-H$ ) show room-temperature ferromagnetism in Q-carbon. There is a finite coercivity ( $\sim 11945$  A/m) of Q-carbon at 300 K. Controlled samples containing only diamond, diamond-like carbon, and sapphire substrate show only diamagnetic behavior, which was subtracted in the represented magnetic plots. The insets in Figure 4a represent a finite coercivity ( $H_c$ ) of  $\sim 15925$  A/m at 10 K (upper inset) and diamagnetic behavior of the as-deposited amorphous carbon grown on c-sapphire substrates (lower inset). The origin of magnetism in Q-carbon can be due to the electronic mixing of  $sp^2$  and  $sp^3$  orbital states during its formation. Q-Carbon is formed by quenching and super undercooling of liquid metallic carbon, which consists of a large fraction of unpaired electrons. Some of these unpaired electrons remain in the Q-carbon structure, which lead to the observed ferromagnetism. In Q-carbon, the ferromagnetism is, therefore, intrinsic in nature without the presence of hydrogen or any other impurities.

Several hypotheses were advanced for this new kind of magnetism (in carbon) without the presence of magnetic ions, due to spin ordering effects with the low dimensionality and Dirac-like electron spectrum.<sup>44</sup> Magnetism in  $sp$  oxides like MgO or in carbon-based materials like graphite is not observed owing to the fact that Stoner criterion suggests less density of delocalized electrons.<sup>7</sup> However, because of the presence of intrinsic defects, ferromagnetism can occur in these materials. Recently room-temperature ferromagnetism in graphene, MgO, and other oxides has been reported.<sup>45–47</sup> So, the mechanism of ferromagnetism in  $s$  and  $p$  electrons for carbon, in contrast to  $3d$  or  $4f$  electrons (in traditional magnets), is quite significant and very interesting. At room temperature (300 K) as well as at low temperature (10 K), all the Q-carbon samples exhibit hysteresis loops in  $M-H$  data indicating the presence of a long-range ferromagnetic ordering in this structure. The hysteresis loops open at low fields, and magnetization seems to approach

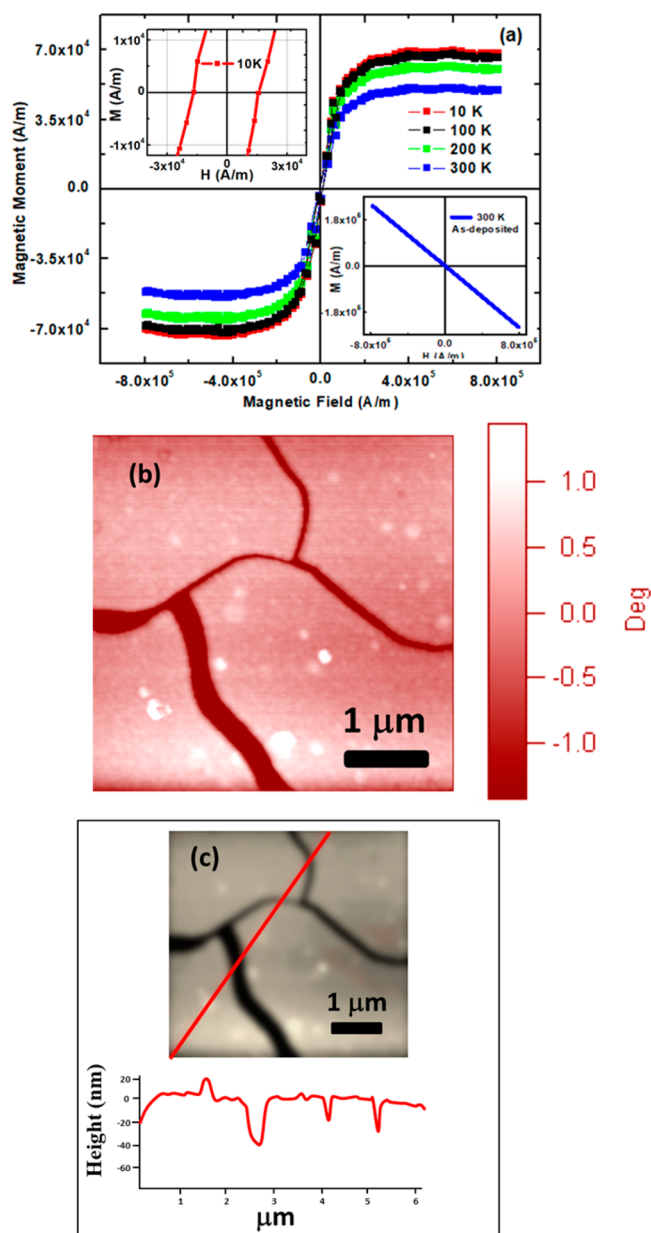


**Figure 4.** (a)  $M-H$  plots of Q-carbon at various temperatures with the insets indicating finite coercivity at 10 K and diamagnetic property of the as-deposited amorphous carbon thin film; (b) MFM image showing distinct magnetic phases of Q-carbon and the rest of the film; and (c) AFM of Q-carbon along with DLC.

a saturation value above 1500 Oe. The  $H_c$  of all samples increases with decreasing temperature. This indicates an increase in the number of active magnetic pinning centers at lower temperatures. To further explore the ferromagnetism in Q-carbon, we also estimated the Curie temperature by extrapolation of the steepest portion of the square of the high field magnetization versus temperature ( $M^2$  vs  $T$ ) plots, which are discussed below. Figure 4b shows a phase-contrast MFM image of Q-carbon along with diamond and DLC at 300 K. The phase-detection mode measures shift in the phase of cantilever oscillation in MFM imaging to minimize the optical interference effects during data acquisition. The change in the phase is caused by magnetic interactions of the tip with the sample surface. The change in phase ( $\Delta\theta$ ) is represented by the following eq 1:

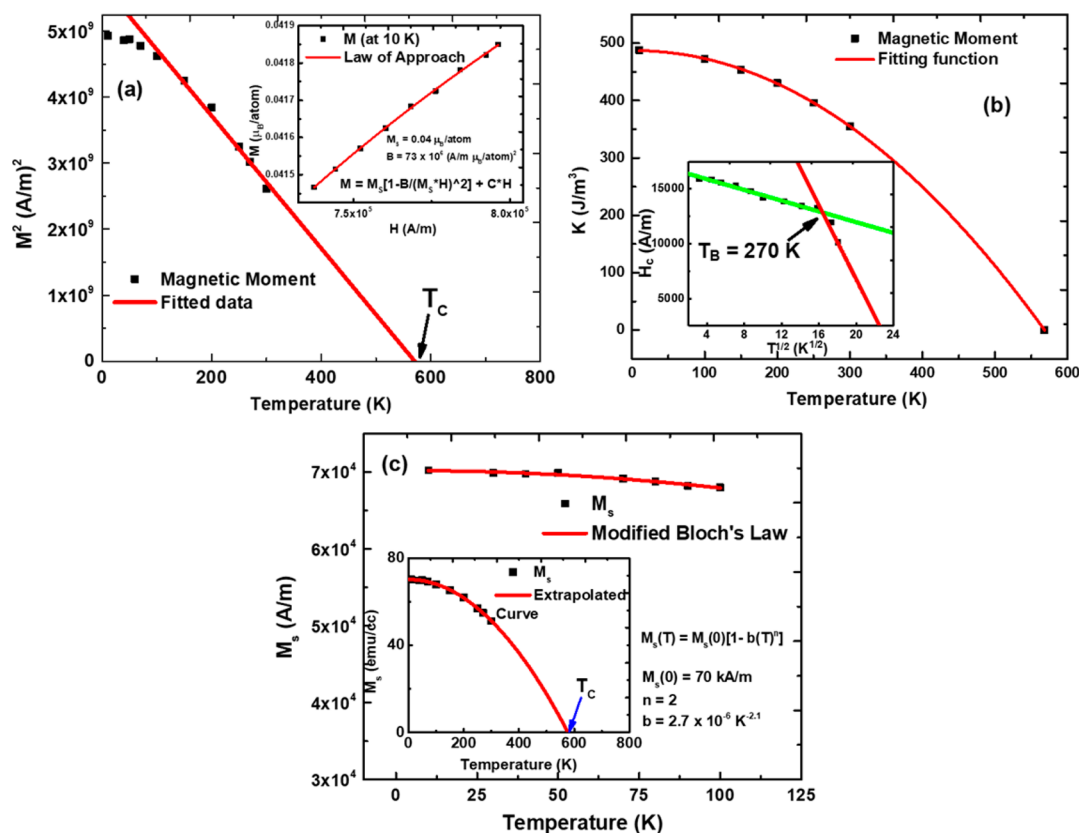


**Figure 5.** (a) Temperature-dependent square of magnetic moment with the linear extrapolation indicating a  $T_c$  of 568 K with the inset showing the LA fitting at 10 K; (b) temperature-dependent magnetic anisotropy with the inset showing  $H_c(\sqrt{T})$  dependence; and (c) modified Bloch's law indicating a Bloch exponent of 2.03 with the inset showing  $T_c \approx 570$  K.

$$\Delta\theta \approx \frac{Q}{k}F \quad (1)$$

where  $Q$ ,  $k$ , and  $F$  denote quality factor, stiffness (of the cantilever), and the vertical force on the cantilever. With the increase in the vertical force on the cantilever, there occurs an increase in the contrast of the phase image acquired in MFM. In general, attractive interactions cause a negative phase shift (dark image contrast), and repulsive interactions cause a positive phase shift (bright image contrast). As it is evident from the AFM (Figure 4c), there occurs a shrinkage of  $\sim 40$  nm when the Q-carbon forms. As it is evident from the MFM image in Figure 4b, Q-carbon has an attractive interaction with the magnetic tip as compared to DLC or diamond. This difference in the phase contrast indicates a ferromagnetic nature of Q-carbon as compared to the rest of the film. The absence of any antisymmetric contrast in the MFM image rules out the possibility of any topographic features (short-range interactions) related artifacts in the magnetic response. The magnetic force microscopy measurements clearly demonstrate that Q-carbon is highly magnetic, and the interface between diamond or DLC and Q-carbon exhibits magnetic contrast at 300 K, while diamond crystallites and DLC are found to be diamagnetic in nature.

Figure 5a shows the linear extrapolation of the  $M^2$  versus  $T$  plot. Curie temperature of the Q-carbon sample is calculated as 570 K, in close agreement with the previously reported value.<sup>23</sup> We used the “Law of Approach (LA)” to determine the temperature-dependent magneto-crystalline anisotropy constant  $K(T)$  and temperature-dependent saturation magnet-

ization  $M_s(T)$ , which is discussed later in this section.<sup>48</sup> The magnetization of a material can be represented<sup>48</sup> by eq 2

$$M = M_s \left( 1 - \frac{8K^2}{105\mu_0^2 M_s^2 H^2} \right) + cH \quad (2)$$

where  $M$  is the magnetization,  $H$  is the applied magnetic field,  $M_s$  is the saturation magnetization,  $\mu_0$  ( $4\pi$  in CGS;  $4\pi \times 10^{-7}$  in SI unit) is the magnetic permeability of free space,  $K$  is the magnetic anisotropy constant, and  $c$  is the linear constant term. The contribution of the linear term  $cH$  is small compared to the first term at large magnetic fields. The term  $B$  in the inset of Figure 5a equals  $8K^2/105\mu_0^2$ . The temperature dependence of  $K(T)$  and  $M_s(T)$  are extracted by fitting the values of magnetization corresponding to the high magnetic field part of the curve, that is, from the saturated portion of the magnetization curve to eq 2.

For the fitting process, only magnetization data above 700 kA/m are used. The fit to eq 2 is shown in the inset of Figure 5a. As represented in Figure 5b, the value of magnetic anisotropy constant decreases with increasing temperature. The values of  $K$  are calculated as  $4.8 \times 10^2$  and  $3.5 \times 10^2$  J/m<sup>3</sup> at 10 and 300 K, respectively. The magnetic anisotropy constant plays an important role in determining the relaxation behavior in magnetic materials. The anisotropy energy restricts the rotation of magnetic moments away from the easy magnetization axis. Therefore, the thermal energy at higher temperatures assists in reducing the value of  $K$  in the Q-carbon structure. The nonlinear dependence of magnetic anisotropy with temperature in Q-carbon can be due to the presence of an

electronic mixture of  $sp^2$ – $sp^3$  hybridized states. From the established theories on magnetic anisotropy as proposed by Van Vleck and Zener,<sup>49,50</sup> the value of correlation exponent in Q-carbon is calculated as 1. This qualifies Q-carbon to be a uniaxial ferromagnet. The solid curve in Figure 5b is the fit to eq 3<sup>51</sup>

$$K(T) = K(0) \left[ 1 - \left( \frac{T}{T_c} \right)^n \right] \quad (3)$$

where  $K(0)$  denotes the magnetic anisotropy at 0 K. The values of  $K(0)$  and  $n$  are calculated as  $0.49 \times 10^3 \text{ J/m}^3$  and 2.045, respectively. The value of the exponent ( $n$ ) is also verified by the modified Bloch's law in Q-carbon, where the Bloch exponent is calculated to be 2.039 and is discussed below in detail. The  $H_c(\sqrt{T})$  dependence in Q-carbon (as shown in the inset of Figure 5b) depicts the ensemble of oriented uniaxial ferromagnetic domains<sup>52–54</sup> (in Q-carbon) magnetized by an external magnetic field. The low-temperature and high-temperature regions signify the blocking and interaction effects, respectively.<sup>54</sup> The blocking temperature ( $T_B$ ) is calculated to be 270 K from the intersection point ( $\sqrt{T_B}$ ) of the two regions. The fact that  $H_c(\sqrt{T})$  dependence has two linear regions indicates the presence of ferromagnetic interparticle interaction in the ensemble. This interaction leads to the formation of a homogeneous ferromagnetism<sup>54</sup> in Q-carbon. Additional magnetic measurements, namely, NMR, ferromagnetic resonance (FMR), and muon spin resonance ( $\mu$ SR) spectroscopy, are an exhaustive study in itself and will be performed (and reported) in near future to determine the homogeneous nature of ferromagnetism in Q-carbon.

The temperature dependence of the saturation magnetization for the case of a continuous distribution of spin-wave states can be well-fitted to the Bloch's theory and is represented by eq 4:<sup>51,55</sup>

$$M_s(T) = M_s(0) \left[ 1 - b \left( \frac{T}{T_c} \right)^n \right] \quad (4)$$

where  $M_s(0)$  is the magnetization of the ground state at  $T = 0$  K,  $b$  is Bloch's constant,  $n$  is the Bloch exponent, and  $T_c$  is the Curie temperature. As shown in Figure 5c, the temperature-dependent saturation magnetization  $M_s(T)$  obtained by fitting to eq 4 decreases with increasing temperature. The values of saturation magnetization for undoped Q-carbon are calculated as 70 and 51 kA/m at 10 and 300 K, respectively. The calculated parameter  $\alpha = b/(T_c)^n$  is  $\sim 1 \times 10^{-6} \text{ K}^{-n}$ . The low values of  $\alpha$  indicate an increase in the spin-wave stiffness coefficient, thereby increasing the spin-wave excitation energy required to switch the spin states in Q-carbon. The value of Bloch exponent varies slightly from 2.039 to 2.042 in the Q-carbon samples. The Bloch's law suggests that the decrease in the saturation magnetization with increasing temperature is due to spin-wave excitations and can be described by a power law in  $T$ .

However, the magnitude of  $M_s$  in the Q-carbon structure may depend on the solidification rates. The Bloch constant is inversely proportional to  $D^n$ , where  $D$  is the coefficient of spin-wave stiffness. The excitation energy  $E_k$  of spin wave in the limit of small wave vectors ( $k \rightarrow 0$ ) is expressed by eq 5:<sup>56</sup>

$$E_k = Dk^2 \quad (5)$$

The finite size of the particles leads to a discrete set of energy values corresponding to a discrete spectrum of the spin-wave modes. In case of a cubic particle with side  $d$ , the spin-wave energies can be roughly estimated using eq 6:<sup>56</sup>

$$E_k = D \left( \frac{n\pi}{d} \right)^2 \quad (6)$$

where  $n$  is an integer. An increase in the value of  $b$  represents a decrease in the spin-wave stiffness constant, and thereby less spin-wave excitation energy  $E_k$  is required to demagnetize ferromagnetic materials at temperatures well-below the transition temperature by the process of excitation of long-wavelength spin waves. It can also be inferred from the eq 6 that a decrease in lattice parameter increases the spin-wave excitation energy. Q-Carbon is formed after melting and subsequent quenching of liquid carbon. This leads to an  $\sim 5\%$  decrease in the C–C bond length in the Q-carbon structure as compared to diamond,<sup>19</sup> which can affect the values of  $E_k$ .

Generally, super-paramagnetism is observed in the case of miniature-sized ferromagnetic or ferrimagnetic nanoparticles. In these materials, the magnetization randomly flips direction with an increase in thermal energy. The magnetization curves of Q-carbon can be explained on the basis of the theory of super-paramagnetic relaxation, assuming that the atomic magnetic moments inside the clusters are parallel.<sup>57</sup> The Bloch exponent is a structure-independent parameter but is dependent on the magnetic domain size. The Bloch constant depends on the effective coordination number  $z_{\text{eff}}$  in the ferromagnetic material. The effective coordination number depends critically on the structure of the outermost shells in the cluster (the cluster closure) as well as on the cluster size. Smaller  $b$  values correspond to "closed" magnetic clusters. According to Linderoth et al.,<sup>58</sup> magnetization may not follow the Bloch's  $T^{3/2}$  law in all ferromagnetic materials. The temperature-dependent saturation magnetization curve in Q-carbon can be fitted (as shown in Figure 5c) using the modified Bloch's law, where the value of the Bloch exponent ( $n$ ) is equal to 2.04 and a prefactor of  $3.02 \times 10^{-6} \text{ K}^{-2.04}$ . Therefore, the temperature-dependent saturation magnetization behavior in Q-carbon can be ascribed to the finite size effects in the spin-wave spectrum. The finite size might also affect electronic properties, resulting in exchange energy constants that vary with position and site-dependent magnetic moments in Q-carbon thin films. The change in magnetization with temperature raised to the calculated mean of Bloch exponent for all the Q-carbon samples follows a linear trend. This linear dependence also corresponds to the pristine nature of samples and instills confidence about the magnetization data acquisition and the analysis technique.

Figure S1a shows  $M$ – $H$  isotherms at various temperatures between 10 and 300 K. As it is evident from the plots, the magnetic moment for all the temperatures remain parallel to the  $H$ -axis. Generally, above the Curie temperature, the isotherms will become straight lines passing through the origin.<sup>59</sup> Since the Curie temperature of the Q-carbon samples are much above 300 K, no such trend was observed in the  $M$ – $H$  isotherms. The linearity is also not observed in the Arrott plots ( $M^2$  vs  $H/M$ ) and is shown in Figure S1b. The value of  $T_c$  is calculated as 630 K. This value is  $\sim 60$  K (11%) higher than that calculated from Bloch's Law. This difference is because Arrott plot is based on Weiss molecular field theory of the ferromagnetism, and therefore it can only be elegantly applied

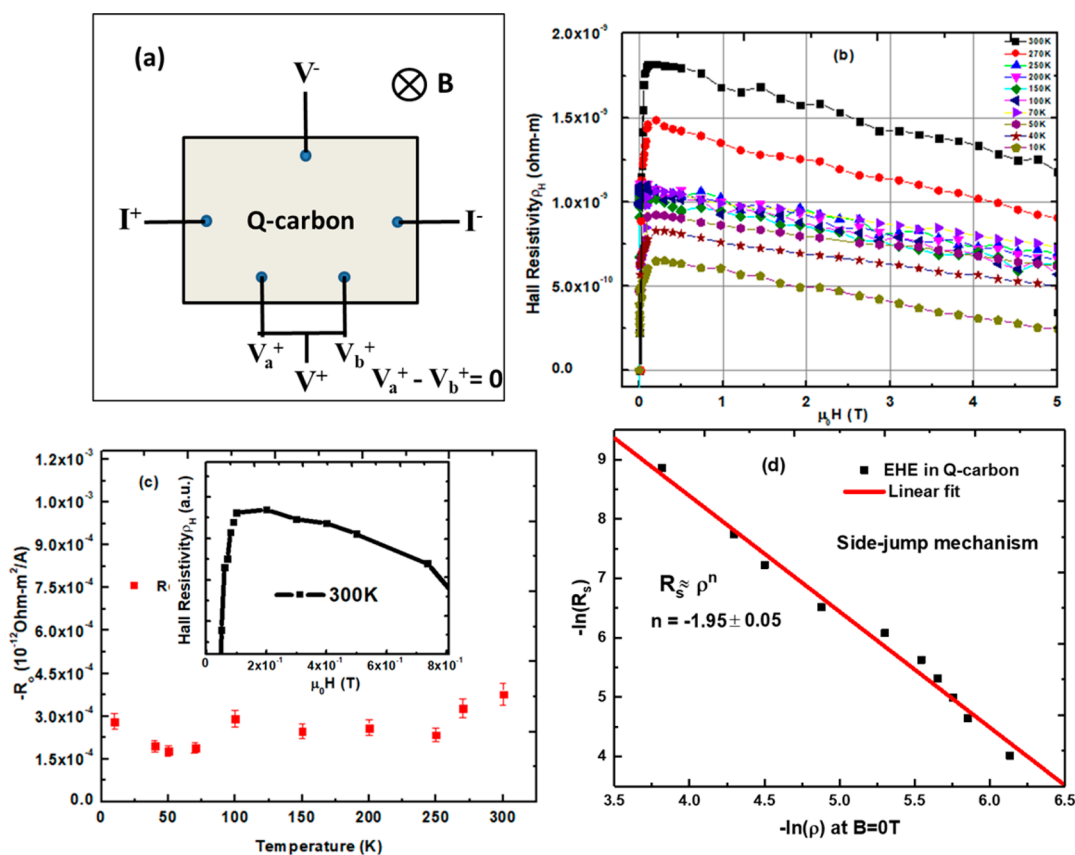


**Figure 6.** (a) Five-probe electrical connection (with nulling of offset voltage) for EHE measurements; (b) Hall resistivity vs magnetic induction plots in Q-carbon at various temperatures; (c) temperature-dependent ordinary Hall coefficient indicating that the electron band is more conducting than the hole band in Q-carbon; and (d) linear fit of  $-\ln(R_s)$  vs  $-\ln(\rho)$  plot with a slope of  $-1.95$  indicating a “side-jump” non-classical electronic scattering mechanism in Q-carbon.

to ferromagnetic materials having low Curie temperature. The discrepancy of  $\sim 11\%$  is due to presence of critical fluctuations that are present in the mean-field calculations (whereas absent in the spin-waves calculation: Bloch’s law). The high-temperature magnetization experiments ( $T \gg T_c$ ) are being pursued, and the same will be reported at a later date. The magnetization measurements at higher temperatures through the critical region (in the vicinity of  $T_c$ ) and up to 1000 K (paramagnetic region) is a study in itself and would certainly facilitate better estimation of  $T_c$  in Q-carbon.

Figure 6a–d represents the extraordinary Hall effect configuration and measurements in Q-carbon. These measurements provide a better understanding of the ferromagnetic state and elucidate the dominant scattering process in this new and exotic phase of carbon. The phenomenological expression for the Hall resistivity of magnetic metals and their dilute alloys can be written as

$$\rho_H = R_0 B + \mu_0 R_s M_S \quad (7)$$

where  $R_0$  is the ordinary Hall coefficient  $(= 1/ne)$  for a single electron or hole band but involves mobilities as well for two-band or multiband metals,  $R_s$  is the extraordinary or the anomalous Hall coefficient,  $B$  is the magnetic field, and  $M$  is the magnetization. In eq 7, the first term represents the ordinary Hall effect, and it results from the Lorentz force acting on the moving charge carriers under the influence of an external magnetic field, while the second term represents the

extraordinary or the anomalous Hall effect, which originates from the spin–orbit interaction in a ferromagnet.

There exist several models in the literature about the origin of the extraordinary Hall effect (EHE).<sup>60–62</sup> In some models the conduction electrons are assumed to be magnetic, and the scattering centers are nonmagnetic, while in other models it is just the opposite. But in all the cases the spin–orbit coupling between the conduction electrons and the scattering centers were considered as the basic mechanism causing the EHE. It is a characteristic property of a ferromagnetic material and is proportional to the magnetization of the sample.

The origin of the extraordinary Hall coefficient  $R_s$  has been understood in terms of the left–right asymmetry in the differential scattering cross-section of the conduction electrons leading to the anomalous Hall effect. Usually  $R_s$  is much larger than  $R_0$ , and it has a strong dependence on the temperature as well as on the impurity concentration. For a ferromagnetic material, both theoretically and experimentally,  $R_s$  is found to have a power law relation with the longitudinal Ohmic resistivity  $\rho$  and is given by  $R_s = a\rho + b\rho^2$ , where  $\rho$  is the bulk resistivity, and  $a$  and  $b$  are constants that are the characteristics of the material itself. The linear term in  $\rho$  is attributed to the Smit asymmetric scattering or the skew scattering of the charged carriers, derivable from the classical Boltzmann equation, while the quadratic term in  $\rho$  is attributed to the side-jump mechanism proposed by Berger.<sup>63</sup> This is purely a quantum mechanical effect. Both the scattering phenomena mentioned above have their origin in the spin–orbit interaction present in a ferromagnet. On the one hand,

the skew scattering shows up for pure materials at low temperatures. On the other hand, the side-jump scattering is dominant for impure and disordered materials or at high temperatures. This nonclassical transport is most commonly seen in Fe–Cr and other concentrated alloys.<sup>61,62</sup> Figure 6b depicts the variation of Hall resistivity with magnetic field at various temperatures (from 10 to 300 K). It shows an initial steep rise of the Hall resistivity at low fields followed by small negatively sloped characteristics at high fields that exhibit nearly saturation behavior as observed in a ferromagnetic material. As it is evident from the Figure 6b, there is a minimal change in the slope of Hall resistivity at high fields in the Q-carbon structure. This is due to a minimal change in the conductivities of the electron and hole bands.<sup>61</sup> The negative slopes of the  $\rho_H$  versus  $B$  plots indicate an n-type conductivity in Q-carbon in the entire temperature range from 10 to 300 K. The decrease of Hall resistivity with an increase in the applied magnetic field in Q-carbon can be due to the quenching of the long wavelength magnons. In Figure 6c we plotted the change in  $R_0$  with temperature (with error bars) in Q-carbon.  $R_0$  shows an overall increasing trend with the increase in temperature. The negative values of  $R_0$  are because the electron band is the dominant conduction channel than the hole band in Q-carbon. There is also a minimal change in the conductivity over a wide range of temperature (10 to 300 K). There is a considerable change in the values of the intercept in Figure 6b.  $R_H$  can be extracted by dividing the intercepts by  $\mu_0 M_S$ .  $M_S$  is calculated from the modified Bloch's law eq 4 in Q-carbon. The low-field region of the Hall resistivity at 300 K is shown as an inset in Figure 6c. It is clearly observed that there occurs an onset of saturation at  $\sim 1000$  Oe (0.1 T), which is consistent with the  $M$ – $H$  hysteresis loop (at 300 K) in Q-carbon. In Figure 6d we plotted  $-\ln(R_S)$  versus  $-\ln(\rho)$ . The calculated slope ( $n$ ) of the linear fit in Figure 6d is 1.95. This value of  $n$  is very close to the prediction of quantum transport theory, where  $R_S \propto \rho^2$ .<sup>63</sup> The side-jump mechanism exists in Q-carbon due to the presence of scattering centers that distort the wave function and create a local current density. However, in the case of disordered dilute alloys and Q-carbon the scattering centers are located far from each other; thereby, the outgoing scattered waveforms lack a definite phase relationship.

The structure–property correlations of Q-carbon lead to a better understanding of the interesting magnetic and electron-transport properties. The formation of Q-carbon is dependent on the laser parameters and physical properties of the substrate, which control the solidification velocity. The solidification velocity ( $v$ ) is directly related to the undercooling by eq 8:<sup>64</sup>

$$v = \frac{D_\infty f}{\lambda f_D} (1 - e^{\Delta G/kT}) \quad (8)$$

where,  $D_\infty$ ,  $f$ ,  $\lambda$ ,  $f_D$ ,  $\Delta G$ ,  $k$ , and  $T$  denote diffusivity of the amorphous carbon, fraction of the available sites, atomic jump distance, geometrical factor associated with diffusion ( $\sim 1$ ), chemical free energy barrier for amorphous carbon to Q-carbon phase transformation, Boltzmann constant, and temperature, respectively. Again  $\Delta G = (T_m - T_u)\Delta S$ , where  $T_u$  and  $\Delta S$  denote the undercooling temperature and the change in entropy, respectively. Detailed calculations of the variation of undercooling temperatures with the  $sp^3$  fraction in the as-deposited C layer are reported elsewhere.<sup>65</sup> An increase in the value of  $T_u$  decreases the value of chemical free energy barrier for amorphous to Q-carbon phase transformation. This

increases the velocity of the melt front. Therefore, the values of undercooling are a determining factor for the production of Q-carbon from the carbon melt. The thermal conductivity of the as-deposited amorphous carbon film and the substrate also play an important role in the formation of the new phase of carbon. With the increase in the pulse duration, the onset of melting decreases with a decrease in the solidification velocity. The maximum depth of melt also decreases with the increase in the duration of the laser pulse. There is also an increase in the time of peak melt depth with increasing laser pulse width. Calculations also show that the melt depth increases with the increase in substrate (sapphire) temperature. In all of the above-mentioned calculations, the substrate temperature was considered as 300 K. The relatively low plasma frequency of amorphous carbon leads to a better material-laser coupling when 193 nm excimer laser is used. As it is evident from the temperature profile in the Figure 1d, the onset of melting occurs at  $\sim 5$  ns after the laser is incident on the amorphous C structure. A flatter temperature profile with time is essential for a homogeneous growth of Q-carbon structure. The high values of solidification velocity cause a sufficient undercooling to form amorphous Q-carbon on c-sapphire. Note that a larger undercooling is needed to form Q-carbon as compared to diamond.<sup>23</sup> Since Q-carbon is formed by the quenching of molten carbon, there are dangling bonds that contain unpaired electrons. This in turn, leads to ferromagnetism and extraordinary Hall effect in Q-carbon. As evident from the Raman spectrum, the shift in the diamond peak ( $E_{2g}$ ) in Q-carbon is due to the presence of hydrostatic pressure. Up to pressures of 40 GPa, the Raman shift of the diamond peak can be calculated using eq 9:

$$\omega(P) = \omega_0 + a_1 P + a_2 P^2 \quad (9)$$

where  $\omega_0$ ,  $a_1$ , and  $a_2$  are  $1333.0 \text{ cm}^{-1}$ ,  $2.83 \text{ cm}^{-1} \text{ GPa}^{-1}$ , and  $-3.65 \times 10^{-3} \text{ cm}^{-1} \text{ GPa}^{-2}$ , respectively.<sup>37</sup> The hydrostatic pressure calculated using eq 9 in Q-carbon is  $-1.36$  GPa (compressive). This indicates a decrease in the C–C  $\sigma$  bond length in Q-carbon. However, the decrease in C–C bond length is primarily derived from the quenching of molten state. The decrease in the bond length is associated with an increase in hardness and density of the electronic states, which may lead to room-temperature ferromagnetism and extraordinary Hall effect in Q-carbon. The asymmetry near the  $\pi^*$  peak in Q-carbon indicates excitonic distortion due to its semimetallic structure. This indicates a strong Coulomb interaction. A similar kind of “quasi-metallic” nature has also been reported in  $C_{60}$ ,<sup>66</sup> which leads to interesting physical and chemical properties. An increase in the intensity and fwhm of the  $\pi^*$  peak in Q-carbon as compared to the as-deposited DLC or diamond (as it is evident from the Figure 3c), indicate an increase in the electronic density of the dangling bonds (present near the Fermi level). This increase leads to ferromagnetism and non-classical extraordinary Hall Effect mechanism in Q-carbon. When spin imbalances are created only by an external applied magnetic field, the material assumes a paramagnetic state. In the case of Q-carbon, there is a high density of electronic states ( $N(E)$ ) near the Fermi level and strong Coulomb interaction (excitonic distortion). This induces an exchange interaction, which causes spin imbalance, thereby leading to ferromagnetic ordering in accordance with the Stoner criterion for ferromagnetism, which states that

$$I_{\text{ex}} \cdot N(E) > 1 \quad (10)$$

where  $I_{\text{ex}}$  and  $N(E)$  denote exchange integral and electronic density of states at Fermi energy level, respectively. The exchange integral in Q-carbon is calculated using eq 11:<sup>67</sup>

$$I_{\text{ex}} = \frac{3k\theta}{2zS(S+1)} \quad (11)$$

where  $k$ ,  $\theta$ ,  $z$ , and  $S$  denote the Boltzmann constant, Curie temperature, coordination number, and spin quantum number, respectively. The exchange integral in Q-carbon is calculated as  $6.10 \times 10^{-15}$  erg, which is  $\sim 13\%$  of that in Fe ( $4.85 \times 10^{-14}$  erg). These exchange forces are primarily dependent on the interatomic distances and not on the crystalline structure of a material.<sup>54</sup> The exchange integral value in Q-carbon suggests that the exchange energy is minimum when the electron spins are parallel to each other. This magnetic alignment coupled with an increase in the electronic density of states near the Fermi energy level give rise to room-temperature ferromagnetism and extraordinary Hall effect in the amorphous Q-carbon structure.

## CONCLUSION

The field-dependent magnetization plots of Q-carbon confirm a finite coercivity and a saturation magnetization in the temperature range of 10–300 K. The origin of intrinsic ferromagnetism in Q-carbon is due to the electronic mixing of  $sp^2$  and  $sp^3$  orbitals during its formation. Some of the unpaired electrons remain in the Q-carbon structure, which renders it to be ferromagnetic in nature. This is the first direct evidence for bulk intrinsic ferromagnetism in carbon without the presence of hydrogen or any other magnetic impurities. In our carefully conducted experiments, amorphous carbon (as-deposited DLC) with 50%  $sp^2$  and 50%  $sp^3$  is found to be diamagnetic. This amorphous carbon turns magnetic only when it is melted in a super-undercooled state and quenched to form Q-carbon. The high density of states near the Fermi level in Q-carbon (as compared to DLC) is illustrated by EELS. Usually,  $\pi^*$  peak intensity of carbon K-edge increases with increasing  $sp^2$  fraction. Interestingly,  $\pi^*$  peak intensity in Q-carbon is drastically enhanced as compared to parent DLC, in spite of having much lower  $sp^2$  content (20% vs 40% in DLC). The area under the  $\pi^*$  peak can be directly correlated to the density of electronic states near the Fermi level, which is clearly higher in Q-carbon as compared to the DLC and diamond, which are diamagnetic in nature. The temperature-dependent magnetic anisotropy constant calculations in Q-carbon indicate a nonlinear dependence with an exponent value of 2.03 that is attributed to the presence of an electronic mixture of  $sp^2$ - $sp^3$  hybridized states. The temperature-dependent saturation magnetization curve in Q-carbon follows the modified Bloch's law with the Bloch exponent equal to 2.04, prefactor of  $1.0 \times 10^{-6} \text{ K}^{-2.04}$ , and a Curie temperature of 570 K. The negative values of the ordinary Hall coefficient in the temperature range from 10 to 300 K indicate that the electron band is more conducting than the hole band in Q-carbon. An exponent value of  $1.95 \pm 0.05$  has been extracted from the extraordinary Hall Effect calculations in Q-carbon, which suggests that the electron scattering in Q-carbon follows a nonclassical side-jump mechanism. This electronic scattering mechanism exists in Q-carbon due to the presence of nonconducting centers that distort the wave function and create a local current density. There is an increase in the intensity and fwhm of the  $\pi^*$  peak in Q-carbon (as it is evident from the EEL spectrum) as compared

to the as-deposited DLC or diamond. This indicates an increase in the electronic density of the dangling bonds (present near the Fermi level) leading to exciting magnetic and electrical properties in Q-carbon. The coexistence of room-temperature ferromagnetism and extraordinary Hall effect in Q-carbon thin films suggests that the ferromagnetically spin-polarized carriers can indeed be probed and controlled electronically. Our results clearly show that Q-carbon thin films can be used in spintronics-based and various other room-temperature magneto-electronic applications. We envisage that this discovery of room-temperature ferromagnetism and extraordinary Hall effect in Q-carbon will certainly stimulate further research in carbon-based materials.

## ASSOCIATED CONTENT

### Supporting Information

The Supporting Information is available free of charge on the ACS Publications website at DOI: 10.1021/acsanm.7b00253.

The details of Arrott plots in Q-carbon (PDF)

## AUTHOR INFORMATION

### Corresponding Author

\*E-mail: narayan@ncsu.edu.

### ORCID

Anagh Bhaumik: 0000-0002-1043-6364

Ritesh Sachan: 0000-0002-3604-1467

Jagdish Narayan: 0000-0002-0724-7044

### Author Contributions

J.N., A.B., R.S., and S.N. initiated and coordinated the research. S.N., A.B., D.K., and A.K.M. performed the magnetic and extraordinary Hall effect measurements. R.S. performed the HAADF imaging and EELS. A.B. prepared the samples and performed the HRTEM, FESEM, XRD, Raman spectroscopy, and SIMS measurement. S.G. and A.B. performed the SLIM calculations. A.B. wrote the manuscript with inputs from R.S., S.N., J.N., and A.K.M.

### Notes

The authors declare no competing financial interest.

## ACKNOWLEDGMENTS

We are grateful to Fan Family Foundation Distinguished Chair Endowment for J. Narayan and NSF DMR-1735695 grant. R.S. acknowledges the National Academy of Sciences (NAS), United States, for awarding the NRC research fellowship. This work was performed in part at the Analytical Instrumentation Facility (AIF) at North Carolina State Univ., which is supported by the State of North Carolina and the National Science Foundation (Award No. DMR-1560838). D.K. acknowledges the financial support of the Univ. of Nebraska-Lincoln MRSEC Center via Grant No. (NSF-DMR 1420645) and NSF-MPS-DMR (Grant No. 0820521). We are also very pleased to acknowledge the technical help and useful discussions with R. G. Ponnamp, N. R. Mucha, J. Prater, R. Narayan, F. Hunte, and J. Schwartz.

## REFERENCES

- (1) Makarova, T.; Palacio Parada, F. *Carbon-Based Magnetism: An Overview of the Magnetism of Metal Free Carbon-Based Compounds and Materials*; Elsevier, 2006.
- (2) Haddon, R. C. Magnetism of the Carbon Allotropes. *Nature* 1995, 378, 249–255.

- (3) Sepioni, M.; Nair, R. R.; Rablen, S.; Narayanan, J.; Tuna, F.; Winpenny, R.; Geim, A. K.; Grigorieva, I. V. Limits on Intrinsic Magnetism in Graphene. *Phys. Rev. Lett.* **2010**, *105*, 207205–1–4.
- (4) Zhang, G.; Samuely, T.; Xu, Z.; Jochum, J. K.; Volodin, A.; Zhou, S.; May, P. W.; Onufriienko, O.; Kačmarčík, J.; Steele, J. A.; Li, J.; Vanacken, J.; Vacík, J.; Szabó, P.; Yuan, H.; Roeffaers, M. B. J.; Cerbu, D.; Samuely, P.; Hofkens, J.; Moshchalkov, V. V. Superconducting Ferromagnetic Nanodiamond. *ACS Nano* **2017**, *11*, 5358–5366.
- (5) McConnell, H. M. Ferromagnetism in Solid Free Radicals. *J. Chem. Phys.* **1963**, *39*, 1910–1910.
- (6) Mataga, N. Possible “ferromagnetic States” of Some Hypothetical Hydrocarbons. *Theor. Chim. Acta* **1968**, *10*, 372–376.
- (7) Stoneham, M. The Strange Magnetism of Oxides and Carbons. *J. Phys.: Condens. Matter* **2010**, *22*, 074211–1–7.
- (8) Kawabata, K.; Mizutani, M.; Fukuda, M.; Mizogami, S. Ferromagnetism of Pyrolytic Carbon under Low-Temperature Growth by the CVD Method. *Synth. Met.* **1989**, *33*, 399–402.
- (9) Katulevskii, Y. A.; Magrupov, M. A.; Muminov, A. A. A New Magnetic Material: Organic Ferromagnet of Pyrolysed Polyacrylonitrile. *Phys. Status Solidi* **1991**, *127*, 223–229.
- (10) Liu, S.; Zhen, C.; Li, Y.; Pan, C.; Zhou, H.; Hou, D. Ferromagnetism in Hydrogenated N-Doped Amorphous Carbon Films. *Phys. Procedia* **2012**, *32*, 450–455.
- (11) Likodimos, V.; Glenis, S.; Lin, C. L. Electronic Properties of Boron-Doped Multiwall Carbon Nanotubes Studied by ESR and Static Magnetization. *Phys. Rev. B: Condens. Matter Mater. Phys.* **2005**, *72*, 45436–1–7.
- (12) Schilder, A.; Bietsch, W.; Schwoerer, M. The Role of TDAE for the Magnetism in [TDAE]C 60. *New J. Phys.* **1999**, *1*, 5–5.
- (13) Esquinazi, P.; Spemann, D.; Höhne, R.; Setzer, A.; Han, K.-H.; Butz, T. Induced Magnetic Ordering by Proton Irradiation in Graphite. *Phys. Rev. Lett.* **2003**, *91*, 227201–1–4.
- (14) Mizogami, S.; Mizutani, M.; Fukuda, M.; Kawabata, K. Abnormal Ferromagnetic Behavior for Pyrolytic Carbon under Low Temperature Growth by CVD Method. *Synth. Met.* **1991**, *43*, 3271–3274.
- (15) Ugeda, M. M.; Brihuega, I.; Guinea, F.; Gómez-Rodríguez, J. M. Missing Atom as a Source of Carbon Magnetism. *Phys. Rev. Lett.* **2010**, *104*, 096804–1–4.
- (16) Peres, N. M. R.; Guinea, F.; Castro Neto, A. H. Coulomb Interactions and Ferromagnetism in Pure and Doped Graphene. *Phys. Rev. B: Condens. Matter Mater. Phys.* **2005**, *72*, 174406–1–10.
- (17) Wakabayashi, K.; Fujita, M.; Kusakabe, K.; Nakada, K. Magnetic Structure of Graphite Ribbon. *Czech. J. Phys.* **1996**, *46*, 1865–1866.
- (18) Khveshchenko, D. V. Ghost Excitonic Insulator Transition in Layered Graphite. *Phys. Rev. Lett.* **2001**, *87*, 246802–1–4.
- (19) Ferromagnetism Appears in Nitrogen Implanted Nanocrystalline Diamond Films. *J. Magn. Magn. Mater.* **2015**, *394*, 477–480.
- (20) Zhang, X.; Hou, L.; Samori, P. Coupling Carbon Nanomaterials with Photochromic Molecules for the Generation of Optically Responsive Materials. *Nat. Commun.* **2016**, *7*, 11118.
- (21) Narayan, J.; Bhaumik, A. Research Update: Direct Conversion of Amorphous Carbon into Diamond at Ambient Pressures and Temperatures in Air. *APL Mater.* **2015**, *3*, 100702–1–11.
- (22) Bundy, F. P.; Bassett, W. A.; Weathers, M. S.; Hemley, R. J.; Mao, H. U.; Goncharov, A. F. The Pressure-Temperature Phase and Transformation Diagram for Carbon; Updated through 1994. *Carbon* **1996**, *34*, 141–153.
- (23) Narayan, J.; Bhaumik, A. Novel Phase of Carbon, Ferromagnetism, and Conversion into Diamond. *J. Appl. Phys.* **2015**, *118*, 215303–1–12.
- (24) Heremans, J.; Olk, C. H.; Eesley, G. L.; Steinbeck, J.; Dresselhaus, G. Observation of Metallic Conductivity in Liquid Carbon. *Phys. Rev. Lett.* **1988**, *60*, 452–455.
- (25) Narayan, J.; Godbole, V. P.; White, C. W. Laser Method for Synthesis and Processing of Continuous Diamond Films on Nondiamond Substrates. *Science* **1991**, *252*, 416–418.
- (26) Amato, I. Fanning the Hope for Flat Diamond. *Science* **1991**, *252*, 375.
- (27) Narayan, J.; Bhaumik, A. Q-Carbon Discovery and Formation of Single-Crystal Diamond Nano- and Microneedles and Thin Films. *Mater. Res. Lett.* **2016**, *4*, 118–126.
- (28) Donovan, E. P.; et al. Heat of Crystallization and Melting Point of Amorphous Silicon. *Appl. Phys. Lett.* **1983**, *42*, 698–700.
- (29) Narayan, J.; White, C. W. Pulsed Laser Melting of Amorphous Silicon Layers. *Appl. Phys. Lett.* **1984**, *44*, 35–37.
- (30) Narayan, J.; White, C. W.; Holland, O. W.; Aziz, M. J. Phase Transformation and Impurity Redistribution during Pulsed Laser Irradiation of Amorphous Silicon Layers. *J. Appl. Phys.* **1984**, *56*, 1821–1830.
- (31) Bagley, B. G.; Chen, H. S. A Calculation of the Thermodynamic First Order Amorphous Semiconductor to Metallic Liquid Transition Temperature. In *AIP Conference Proceedings*; AIP, 1979; Vol. 50, pp 97–101.
- (32) Bhaumik, A.; Sachan, R.; Gupta, S.; Narayan, J. Discovery of High-Temperature Superconductivity ( $T_c = 55$  K) in B-Doped Q-Carbon. *ACS Nano* **2017**, *11*, 11915–11922.
- (33) Prinz, G. A. Magnetoelectronics. *Science* **1998**, *282*, 1660–1663.
- (34) Matsumoto, Y.; Murakami, M.; Shono, T.; Hasegawa, T.; Fukumura, T.; Kawasaki, M.; Ahmet, P.; Chikyow, T.; Koshihara, S.; Koinuma, H. Room-Temperature Ferromagnetism in Transparent Transition Metal-Doped Titanium Dioxide. *Science* **2001**, *291*, 854–856.
- (35) Wang, Z.; Wang, W.; Tang, J.; Tung, L. D.; Spinu, L.; Zhou, W. Extraordinary Hall Effect and Ferromagnetism in Fe-Doped Reduced Rutile. *Appl. Phys. Lett.* **2003**, *83*, 518–520.
- (36) Singh, R. K.; Narayan, J. A Novel Method for Simulating Laser-Solid Interactions in Semiconductors and Layered Structures. *Mater. Sci. Eng., B* **1989**, *3*, 217–230.
- (37) Prawer, S.; Nemanich, R. J. Raman Spectroscopy of Diamond and Doped Diamond. *Philos. Trans. R. Soc., A* **2004**, *362*, 2537–2565.
- (38) Bhaumik, A.; Sachan, R.; Narayan, J. A Novel High-Temperature Carbon-Based Superconductor: B-Doped Q-Carbon. *J. Appl. Phys.* **2017**, *122*, 045301–1–15.
- (39) Bhaumik, A.; Sachan, R.; Narayan, J. High-Temperature Superconductivity in Boron-Doped Q-Carbon. *ACS Nano* **2017**, *11*, 5351–5357.
- (40) Narayan, J. Interface Instability and Cell Formation in Ion-implanted and Laser-annealed Silicon. *J. Appl. Phys.* **1981**, *52*, 1289–1293.
- (41) Narayan, J.; Bhaumik, A. Novel Synthesis and Properties of Pure and NV-Doped Nanodiamonds and Other Nanostructures. *Mater. Res. Lett.* **2017**, *5*, 1–9.
- (42) Sachan, R.; Cooper, V. R.; Liu, B.; Aidhy, D. S.; Voas, B. K.; Lang, M.; Ou, X.; Trautmann, C.; Zhang, Y.; Chisholm, M. F.; Weber, W. J. Forging Fast Ion Conducting Nanochannels with Swift Heavy Ions: The Correlated Role of Local Electronic and Atomic Structure. *J. Phys. Chem. C* **2017**, *121*, 975–981.
- (43) Bruley, J.; Williams, D. B.; Cuomo, J. J.; Pappas, D. P. Quantitative near-Edge Structure Analysis of Diamond-like Carbon in the Electron Microscope Using a Two-Window Method. *J. Microsc.* **1995**, *180*, 22–32.
- (44) Kuzemsky, A. L. Unconventional and exotic magnetism in carbon-based structures and related materials. *Int. J. Mod. Phys. B* **2013**, *27*, 1330007–1–39.
- (45) Wang, Y.; Huang, Y.; Song, Y.; Zhang, X.; Ma, Y.; Liang, J.; Chen, Y. Room-Temperature Ferromagnetism of Graphene. *Nano Lett.* **2009**, *9*, 220–224.
- (46) Jin, Z.; Nori, S.; Lee, Y.-F.; Kumar, D.; Wu, F.; Prater, J. T.; Kim, K. W.; Narayan, J. Strain Induced Room Temperature Ferromagnetism in Epitaxial Magnesium Oxide Thin Films. *J. Appl. Phys.* **2015**, *118*, 165309–1–6.
- (47) Punugupati, S.; Narayan, J.; Hunte, F. Room Temperature Ferromagnetism in Epitaxial  $\text{Cr}_2\text{O}_3$  Thin Films Grown on R-Sapphire. *J. Appl. Phys.* **2015**, *117*, 193907–1–5.
- (48) Chikazumi, S.; Graham, C. D.; Chikazumi, S. *Physics of Ferromagnetism*; Oxford University Press, 1997.

- (49) Van Vleck, J. H. On the Anisotropy of Cubic Ferromagnetic Crystals. *Phys. Rev.* **1937**, *52*, 1178–1198.
- (50) Zener, C. Classical Theory of the Temperature Dependence of Magnetic Anisotropy Energy. *Phys. Rev.* **1954**, *96*, 1335–1337.
- (51) Wang, J.; Duan, H.; Lin, X.; Aguilar, V.; Mosqueda, A.; Zhao, G. Temperature Dependence of Magnetic Anisotropy Constant in Iron Chalcogenide  $\text{Fe}_3\text{Se}_4$ : Excellent Agreement with Theories. *J. Appl. Phys.* **2012**, *112*, 103905–1–5.
- (52) Timopheev, A. A.; Ryabchenko, S. M.; Kalita, V. M.; Lozenko, A. F.; Trotsenko, P. A.; Stephanovich, V. A.; Grishin, A. M.; Munakata, M. The Influence of Intergranular Interaction on the Magnetization of the Ensemble of Oriented Stoner–Wohlfarth Nanoparticles. *J. Appl. Phys.* **2009**, *105*, 83905.
- (53) Timopheev, A. A.; Ryabchenko, S. M.; Kalita, V. M.; Lozenko, A. F.; Trotsenko, P. A.; Grishin, A. M.; Munakata, M. Effect of Interaction in the Magnetization Reversal Relaxation of Superparamagnetic Granular  $\text{CoFeB}/\text{SiO}_2$  Films. *Solid State Phenom.* **2009**, *152–153*, 213–216.
- (54) Timopheev, A. A.; Bdkin, I.; Lozenko, A. F.; Stognei, O. V.; Sitnikov, A. V.; Los, A. V.; Sobolev, N. A. Superferromagnetism and Coercivity in  $\text{Co}/\text{Al}_2\text{O}_3$  Granular Films with Perpendicular Anisotropy. *J. Appl. Phys.* **2012**, *111*, 123915–1–7.
- (55) Nath, T. K.; Sudhakar, N.; McNiff, E. J.; Majumdar, A. K. Magnetization Study of  $\gamma\text{-Fe}_{80-x}\text{Ni}_x\text{Cr}_{20}$  ( $1 \leq x \leq 30$ ) Alloys to 20 T. *Phys. Rev. B: Condens. Matter Mater. Phys.* **1997**, *55*, 12389–12401.
- (56) Senz, V.; Röhlberger, R.; Bansmann, J.; Leupold, O.; Meiwes-Broer, K.-H. Temperature Dependence of the Magnetization in Fe Islands on  $\text{W}(110)$ : Evidence for Spin-Wave Quantization. *New J. Phys.* **2003**, *5*, 47–49.
- (57) Hendriksen, P. V.; Linderöth, S.; Lindgård, P.-A. Finite-Size Modifications of the Magnetic Properties of Clusters. *Phys. Rev. B: Condens. Matter Mater. Phys.* **1993**, *48*, 7259–7273.
- (58) Linderöth, S.; Balcells, L.; Labarta, A.; Tejada, J.; Hendriksen, P. V.; Sethi, S. A. Magnetization and Mössbauer Studies of Ultrafine Fe-C Particles. *J. Magn. Magn. Mater.* **1993**, *124*, 269–276.
- (59) Sudhakar, N.; Ningthoujam, R. S.; Rajeev, K. P.; Gajbhiye, N. S.; Narayan, J. Structural, Magnetic, and Electron Transport Studies on Nanocrystalline Layered Manganite  $\text{La}_{1.2}\text{Ba}_{1.8}\text{Mn}_2\text{O}_7$  System. *J. Nanosci. Nanotechnol.* **2007**, *7*, 965–969.
- (60) Stern, E. A. Faraday Effect in Magnetized Solids. *Phys. Rev. Lett.* **1965**, *15*, 62–66.
- (61) Khatua, P.; Majumdar, A. K.; Hebard, A. F.; Temple, D. Extraordinary Hall Effect in Fe-Cr Giant Magnetoresistive Multilayers. *Phys. Rev. B: Condens. Matter Mater. Phys.* **2003**, *68*, 144405–1–7.
- (62) Sinha, A.; Majumdar, A. K. Extraordinary Hall Effect in Ni-Fe-Cr Ternary Alloys. *J. Appl. Phys.* **1979**, *50*, 7533–7535.
- (63) Berger, L. Side-Jump Mechanism for the Hall Effect of Ferromagnets. *Phys. Rev. B* **1970**, *2*, 4559–4566.
- (64) Narayan, J. Interface Structures during Solid-phase-epitaxial Growth in Ion Implanted Semiconductors and a Crystallization Model. *J. Appl. Phys.* **1982**, *53*, 8607–8614.
- (65) Gupta, S.; Sachan, R.; Bhaumik, A.; Narayan, J. *JOM* [Online early access]. DOI: 10.1007/s11837-017-2714-y. Published Online: Jan 3, 2018. <https://link.springer.com/article/10.1007%2Fs11837-017-2714-y>.
- (66) Sudhakar, N.; Sharma, S. V.; Grigoryan, L. S.; Chand, P.; Majumdar, A. K.; Dutta, P. K.; Samanta, S. B.; Narlikar, A. V. Metallic Islands in Carbon Cluster Films: Doping Fullerenes with Fullerenes. *Phys. Lett. A* **1992**, *170*, 235–238.
- (67) Cullity, B. D.; Graham, C. D. *Introduction to Magnetic Materials*; IEEE/Wiley, 2009.